



OPEN

Widespread irreversible changes in surface temperature and precipitation in response to CO₂ forcing

Soong-Ki Kim¹, Jongsoo Shin¹, Soon-Il An^{1,2}✉, Hyo-Jeong Kim¹, Nari Im¹, Shang-Ping Xie³, Jong-Seong Kug^{2,4} and Sang-Wook Yeh⁵

Some climate variables do not show the same response to declining atmospheric CO₂ concentrations as before the preceding increase. A comprehensive understanding of this hysteresis effect and its regional patterns is, however, lacking. Here we use an Earth system model with an idealized CO₂ removal scenario to show that surface temperature and precipitation exhibit globally widespread irreversible changes over a timespan of centuries. To explore the climate hysteresis and reversibility on a regional scale, we develop a quantification method that visualizes their spatial patterns. Our experiments project that 89% and 58% of the global area experiences irreversible changes in surface temperature and precipitation, respectively. Strong irreversible response of surface temperature is found in the Southern Ocean, Arctic and North Atlantic Ocean and of precipitation in the tropical Pacific, global monsoon regions and the Himalayas. These global hotspots of irreversible changes can indicate elevated risks of negative impacts on developing countries.

Earth's climate system is experiencing an unprecedented warming owing to increased anthropogenic greenhouse gas emissions since the industrial revolution¹. To mitigate global warming, international efforts have been made, such as the Paris Agreement, which aims to limit global warming to well below 2°C (preferably 1.5°C). However, even if greenhouse gas (in particular, long-lived gases, for example, CO₂) concentrations in the atmosphere are restored to pre-industrial levels, the climate may not return to the previous state. In other words, a climate system can follow a distinct trajectory during periods of greenhouse gas emission and removal. Such a path-dependent behaviour is referred to as hysteresis. Similarly, the ability for the climate system to be restored to its initial state is referred to as reversibility. These two properties characterize the ability of the climate system to recover when subjected to variation in CO₂ concentration and are relevant to an understanding of the potential long-lasting impact of anthropogenic CO₂ emissions.

In recent decades, a series of climate reversibility studies have been conducted including the Carbon Dioxide Removal Model Intercomparison Project². Hysteresis and irreversibility were identified in the Atlantic Meridional Overturning Circulation^{3–5}, Antarctica Ice Sheet^{6,7}, El Niño–Southern Oscillation⁸, Intertropical Convergence Zone⁹, East Asian monsoon¹⁰, sea level¹¹ and global mean surface temperature^{12–17} and precipitation^{12,13,18}. These examples raise the question of how hysteresis and reversibility emerge at a regional level beyond the individual climate components. Our perception of climate change is based on a regional scale¹⁹. Therefore, understanding climate hysteresis and reversibility at a regional level is crucial for assessing climate recoverability from the rise of anthropogenic global warming and for designing climate policy²⁰. Despite their importance, the hysteresis and reversibility of regional climate have not yet been clearly addressed so far.

In this Article, we aim to address the following key questions: how do the global patterns of hysteresis and reversibility look; which specific regions of the world exhibit irreversible changes; what is the key mechanism that shapes global hysteresis and reversibility patterns? We specifically focus on the response of two key climatic variables—surface temperature and precipitation—to CO₂ forcing.

For our investigation, we conducted the CO₂ ramp-up and ramp-down experiment using the Community Earth System Model (CESM) with 28 ensemble members. In the experiment, the atmospheric CO₂ concentration level is increased from 367 ppm to 1,468 ppm (four times the initial level) at 1% per year, then decreased back to 367 ppm at the same rate. The details of the experiment can be found in Methods.

Framework to quantify hysteresis and reversibility

A suitable method is required to analyse spatial patterns of hysteresis and reversibility from the experiment results. The key problem is quantifying hysteresis and reversibility for an entire climate trajectory spanning the CO₂ ramp-up and -down scenario. Previous studies have relied on analysis of the difference between two specific periods with the same CO₂ level (for example, refs. ^{12,16,21}). However, this method cannot completely measure the hysteresis and reversibility for an entire duration of the simulation spanning a wide range of CO₂ levels. Here we develop a conceptual framework to quantify climate hysteresis and reversibility.

A trajectory of the climate state (for example, surface temperature or precipitation) under the CO₂ forcing can be represented as a loop in the CO₂ phase space (Fig. 1a). Under the scenario, the CO₂ concentration (F) is increased from the present-day level (F_{present}) to the future peak level (F_{peak}) and restored back to the present-day level (F_{present}). If the system exhibits hysteresis, the climate trajectory

¹Department of Atmospheric Sciences/Irreversible Climate Change Research Center, Yonsei University, Seoul, South Korea. ²Division of Environmental Science and Engineering, Pohang University of Science and Technology (POSTECH), Pohang, South Korea. ³Scripps Institution of Oceanography, University of California San Diego, La Jolla, CA, USA. ⁴Institute for Convergence Research and Education in Advanced Technology, Yonsei University, Seoul, South Korea. ⁵Department of Marine Sciences and Convergence Technology, Hanyang University, ERICA, Ansan, South Korea. ✉e-mail: sian@yonsei.ac.kr

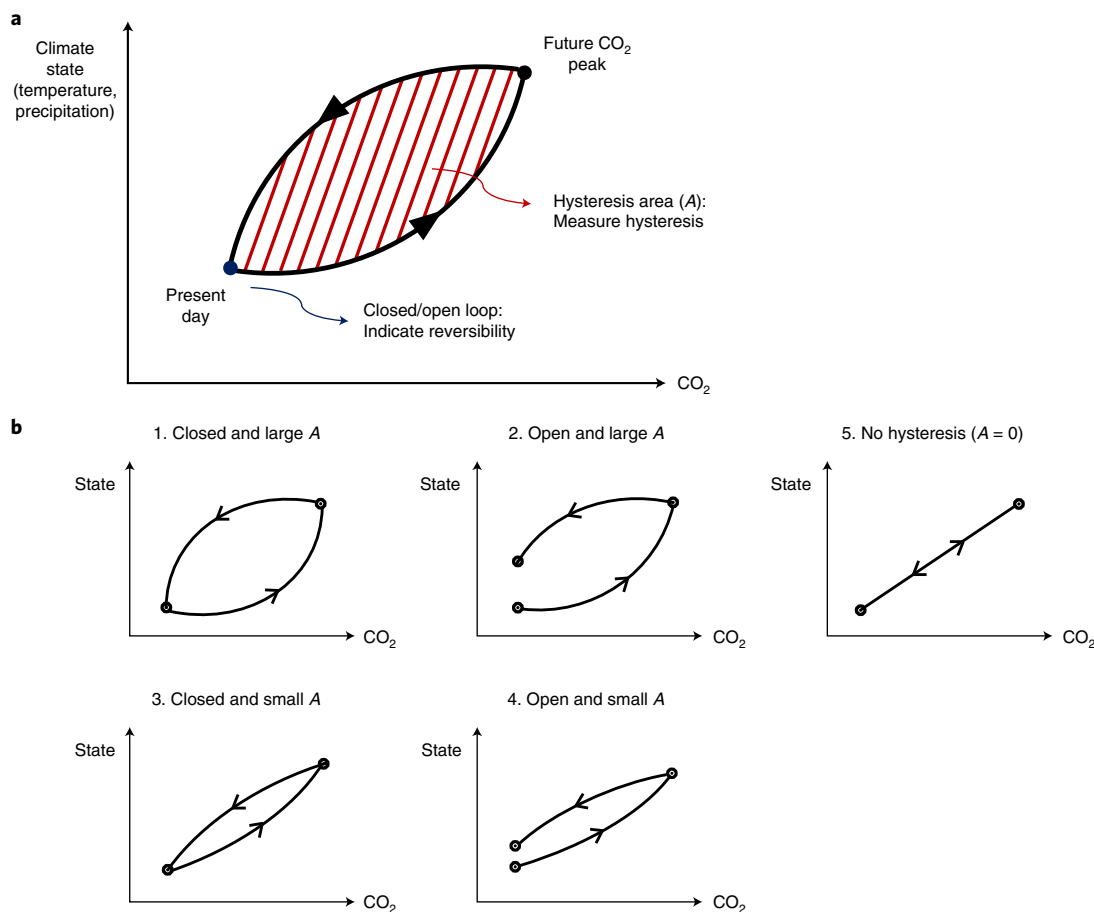


Fig. 1 | The conceptual framework for climate hysteresis and reversibility. **a**, Schematic diagram for the quantitative definition of hysteresis and reversibility. A trajectory of climate state under the CO₂ forcing is shown as black lines. The arrow shows the direction of the trajectory. The hysteresis is measured as the area of the loop (red hatched area). The reversibility is measured as whether the trajectory returned to its initial state as the CO₂ concentration is recovered to the present-day level. **b**, Examples of various types of climate trajectory.

during CO₂ increase (x_{up}) and decrease (x_{down}) would be different. Here hysteresis for the entire trajectory can be measured as the area of the loop, defined as the hysteresis area (A):

$$A = \int_{F_{present}}^{F_{peak}} |x_{down}(F) - x_{up}(F)| dF. \quad (1)$$

The absolute difference between x_{down} and x_{up} holds the hysteresis area always positive. Reversibility of a system can be measured as whether the trajectory return to its initial state, indicated as an open-loop (irreversible change) and closed-loop (reversible change):

$$\text{Loop} = \begin{cases} \text{Open for } x_{down}(F_{present}) \neq x_{up}(F_{present}) \\ \text{Closed for } x_{down}(F_{present}) = x_{up}(F_{present}) \end{cases}. \quad (2)$$

The definitions of hysteresis and reversibility are schematically illustrated in Fig. 1a. These definitions can quantify hysteresis and reversibility as a single scalar value for the entire climate trajectory; therefore, using them, we can map the hysteresis area and openness of the loop for each grid point of the experiment result. The examples of the various types of loop characterized by the hysteresis area and openness are shown in Fig. 1b. If the system has no hysteresis at all, it would exhibit no hysteresis area ($A=0$) and would be closed-loop. It should be noted that the illustrated examples show possible cases of trajectory in a conceptual level. In physical

perspective, all types of loop may not be equally plausible if the hysteresis area and openness are correlated. The detailed physical linkage between them is explained in later parts of the paper.

Note that an open-loop trajectory does not always indicate that a system is completely irreversible. Even if the loop is open, there is a possibility that the system will returns to its initial state if sufficient time is provided after the forcing reaches the initial level²². Nevertheless, at least, they show that the climate system cannot be immediately restored to its initial state even after successful removal of the atmospheric CO₂. The soft definition of irreversibility provides a practical classification for climate recoverability within a human-perceptible timescale.

Hysteresis maps for surface temperature and precipitation

Using the framework, we explore spatial patterns of hysteresis and reversibility in response to CO₂ forcing. We calculated the hysteresis area and loop openness for each grid point of the simulated surface temperature and precipitation. For the loop openness, we applied the refined definition of equation (2), which additionally considers the intersection of loop. The details can be found in Methods. The resultant hysteresis map depicts the hysteresis area as colour shading and hatched regions of a closed-loop response (Figs. 2a and 3a).

The hysteresis map for the surface temperature is presented in Fig. 2a. The hysteresis area of the surface temperature shows large regional differences over the globe. It is the largest in the Southern Ocean near the coast of Antarctica ($A=5,440^\circ\text{C ppm}$)

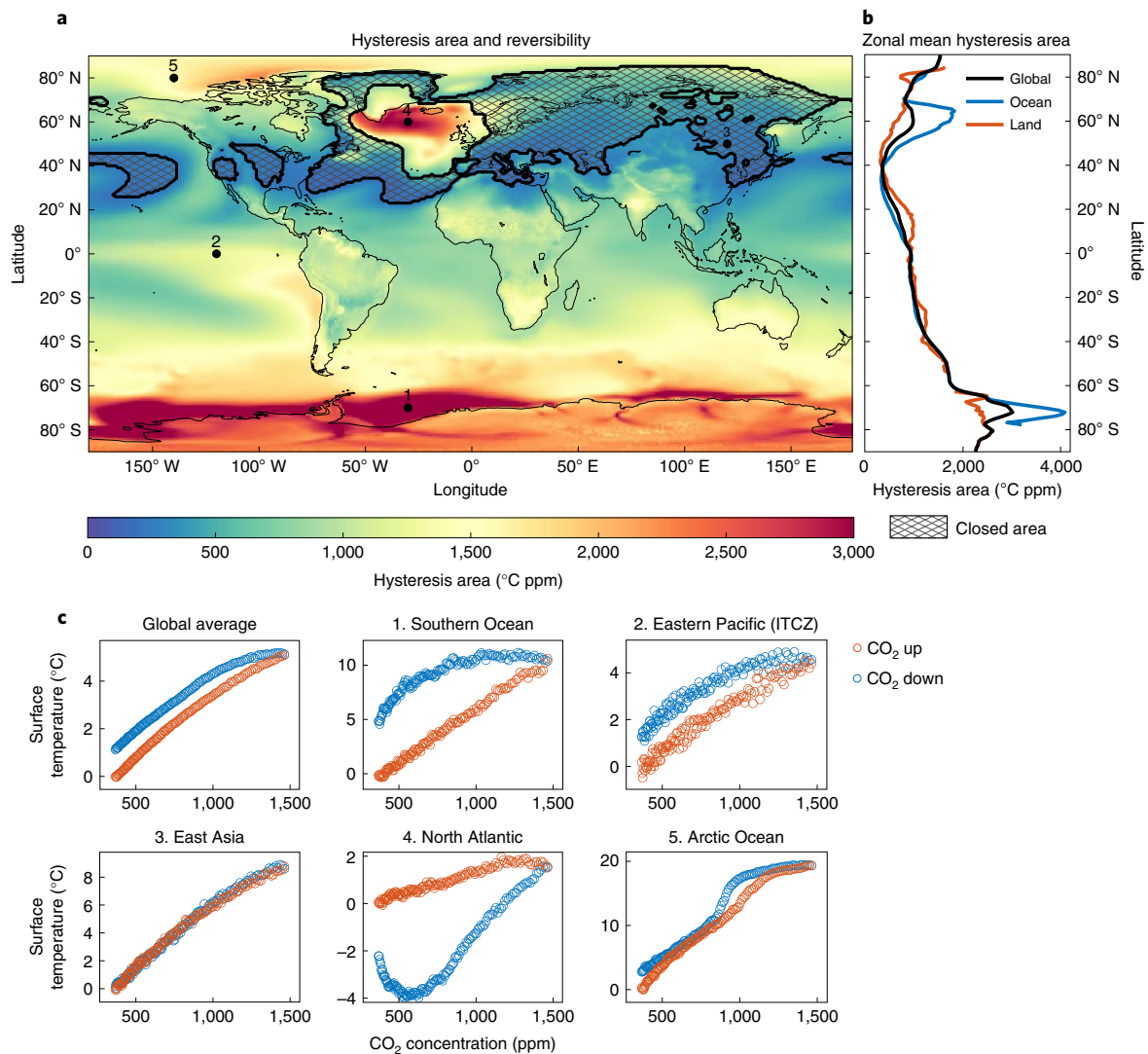


Fig. 2 | Hysteresis and reversibility of surface temperature. **a**, The hysteresis map for surface temperature. The map shows the hysteresis area (unit: $^{\circ}\text{C ppm}$) as colour and the closed-loop region as a hatched pattern. **b**, Zonal mean hysteresis area for the globe (black), ocean (blue) and land (orange). **c**, A trajectory of surface temperature anomaly during a CO_2 ramp-up (orange) and ramp-down (blue) period for selected points. The panels show the Southern Ocean (70°S , 30°W), the eastern equatorial Pacific (0° , 120°W), East Asia (50°N , 120°E), the North Atlantic Ocean (60°N , 30°W), and the Arctic Ocean (80°N , 140°W). The geographical locations are marked as numbered dots in **a**. Additionally, the globally averaged trajectory is presented on the top left side of the panel.

and smallest in the central Atlantic Ocean near the Bermuda islands ($A = 128^{\circ}\text{C ppm}$). Notably, the second-largest hysteresis emerges in the North Atlantic Ocean. The Northern and Southern hemispheres show contrasting responses to CO_2 forcing; the Southern Hemisphere shows larger hysteresis than the Northern Hemisphere (Fig. 2b). The ocean shows a similar hysteresis area to land, but it is exceptionally larger in the North Atlantic Ocean and Southern Ocean (Fig. 2b). Approximately 89% of the total global area show an open-loop response to CO_2 forcing (Fig. 2a). Only specific regions in the northern mid-latitudes and the Arctic show a closed-loop response (~11% of the total global area). This indicates that a vast majority of regions over the globe experience irreversible changes in surface temperature in response to CO_2 forcing. A strong correlation between hysteresis and reversibility is found; the closed-loop (open-loop) regions tend to have a small (large) hysteresis area (Supplementary Fig. 1).

Precipitation shows large regional differences in hysteresis and reversibility (Fig. 3a). The hysteresis area is the largest over the

equatorial tropical Pacific where precipitation is heavily influenced by the Intertropical Convergence Zone²³ ($A = 3,080$ mm per day ppm). Large precipitation hysteresis also emerges in the North Atlantic Ocean, Himalayas and Indonesia. The western Sahara Desert shows the smallest hysteresis ($A = 2.5$ mm per day ppm). The ocean shows a larger globally averaged precipitation hysteresis than land (Fig. 3b). The Northern and Southern hemispheres show a quasi-symmetric distribution in the zonal mean hysteresis area except in the North Atlantic Ocean (Fig. 3b). Approximately 58% of the global area shows an open-loop response for precipitation, and the rest of the 42% shows a closed-loop response (Fig. 3a). Thus, roughly half of the global area experiences irreversible changes in precipitation to CO_2 forcing, and the other half is reversible. The closed-loop response emerges in the Arctic, northern mid-latitude regions and Australia, and the open-loop response emerges in the equatorial tropical Pacific, Southern Ocean and Antarctica (Fig. 3a). Unlike the surface temperature, there is no distinct correlation between the hysteresis area and the openness of the loop (Supplementary Fig. 1).

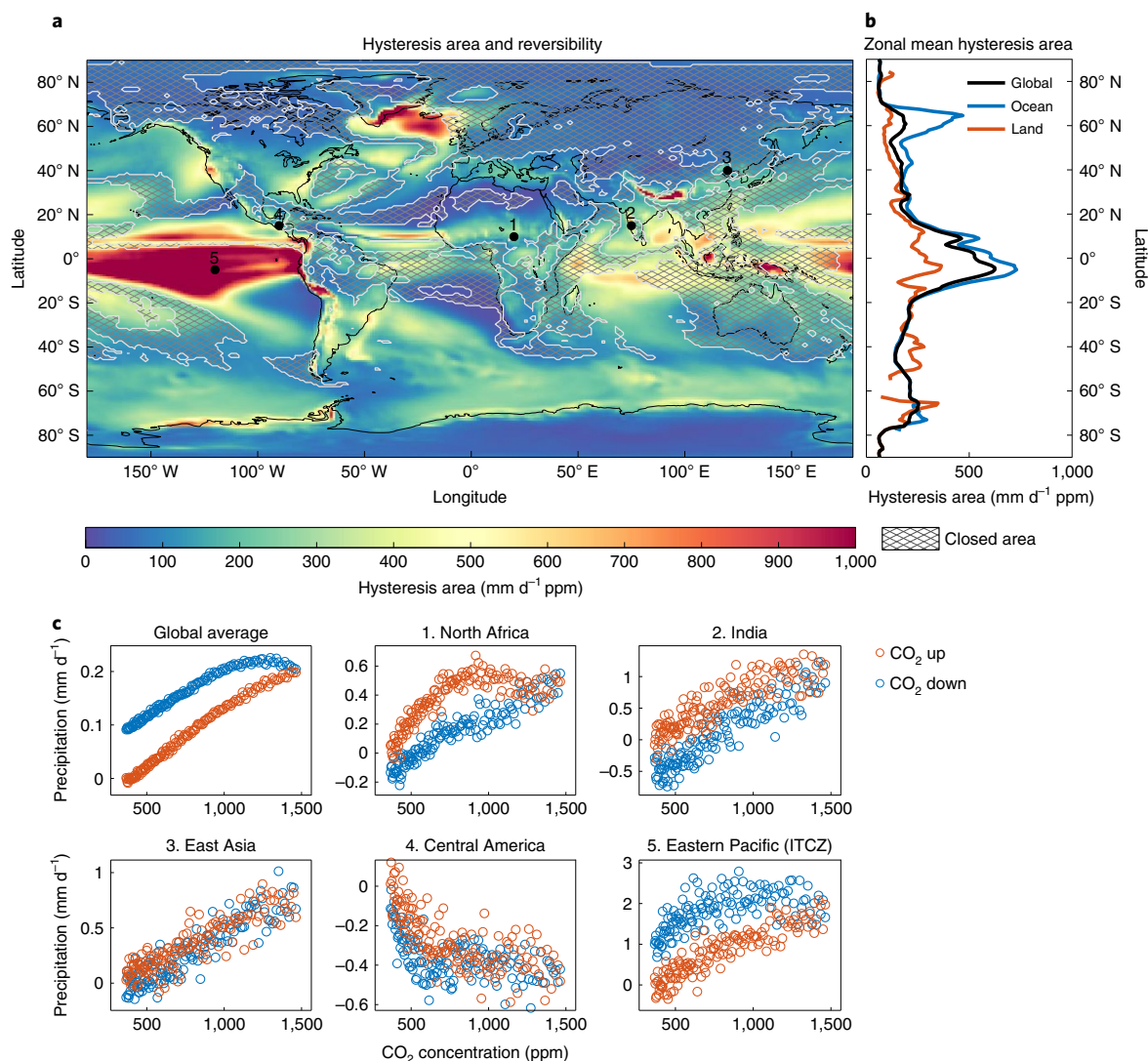


Fig. 3 | Hysteresis and reversibility of precipitation. **a**, The hysteresis map for precipitation. The map shows the hysteresis area (unit: $\text{mm d}^{-1} \text{ppm}$) as colour and the closed-loop region as a hatched pattern. **b**, Zonal mean hysteresis area for the globe (black), ocean (blue) and land (orange). **c**, A trajectory of precipitation anomaly during a CO_2 ramp-up (orange) and ramp-down (blue) period for selected points. The panels show northern Africa (10°N , 20°E), India (15°N , 75°E), East Asia (40°N , 120°E), Central America (15°N , 90°W) and the eastern equatorial Pacific (5°S , 120°W). The geographical locations are marked as numbered dots in **a**. Additionally, the globally averaged trajectory is presented on the top left side of the panel.

To consider the seasonality of surface temperature and precipitation, we additionally calculated a hysteresis map for boreal summer and boreal winter (Supplementary Figs. 2–5). Compared with the annual pattern, the boreal summer and winter patterns for surface temperature hysteresis are different. The hysteresis area is increased in North Africa and India for boreal summer (Supplementary Fig. 2); and the Amazon rainforest and islands in the Arctic for boreal winter (Supplementary Fig. 3). In particular, the Arctic shows strong seasonal contrast in hysteresis and reversibility. The seasonal precipitation patterns also differ from the annual mean. In particular, it highlights irreversible response in global monsoon regions. A large hysteresis and open-loop response of precipitation emerges in India, Southeast Asia, East Asia and Northern Africa for boreal summer (Supplementary Fig. 4) and in western and eastern United States and western South America, southern Africa and Southeast Asia for boreal winter (Supplementary Fig. 5).

Hotspots of irreversible changes

Focusing on comprehensive response in climate variables, we identified hotspots of irreversible climate changes over the land based on

the quantified hysteresis and reversibility. The hotspot for irreversible climate change is defined as a land region where both surface temperature and precipitation show an open-loop response with a large hysteresis area (Methods provide detailed criteria).

The hotspot map is presented in Fig. 4. Under our idealized CO_2 forcing scenario, the hotspots emerge in most developing countries²⁴ located in South America and Africa, such as Chile, Venezuela, Brazil, Nigeria, Ethiopia and Zimbabwe. Developing countries in Central America and South Asia are also classified as the hotspots. In contrast, only a few developed countries²⁴ are classified as the hotspots, such as Ireland and New Zealand. The contrast between developing and developed countries implies a strong regional inequality in climate reversibility to anthropogenic global warming. The strong irreversible changes in developing countries translate into the long-lasting impact of anthropogenic CO_2 emissions, which would vastly increase the risks of climate change with great social costs^{25–27}.

The hotspots also emerge in the regions covered with ice sheets, coastal regions of Antarctica, Greenland and Alaska. Large hysteresis and irreversible changes in these regions can potentially

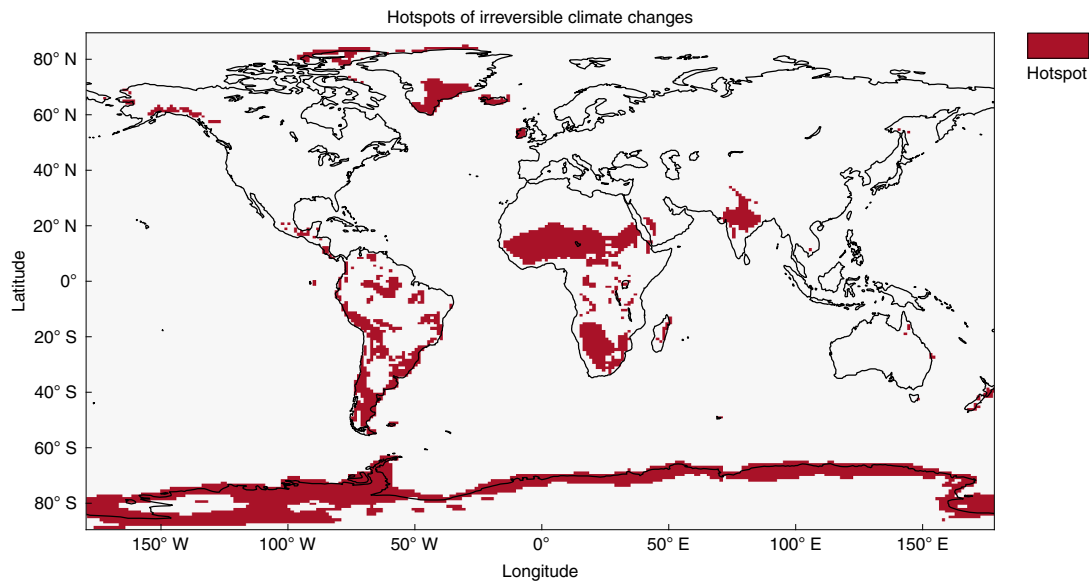


Fig. 4 | Hotspots of irreversible changes. The identified hotspots for irreversible changes are marked in red. A hotspot is defined as the land area where both surface temperature and precipitation show an open-loop response (irreversible change) and a large hysteresis area (>50th percentile) to the CO_2 forcing.

cause the hysteresis in ice sheets^{7,28,29} and marine ecosystems^{30,31}. The polar hotspots highlight the irreversibility of polar regions to CO_2 emissions.

Mechanism of hysteresis and reversibility

The detailed mechanisms for hysteresis and reversibility of surface temperature and precipitation are regionally dependent. For example, the large surface temperature hysteresis in the Southern Ocean is possibly related to warming delay effect mainly caused by the strong Ekman upwelling of the cold deep ocean water and heat uptake by the deep ocean^{32–34}. The large precipitation hysteresis over the tropical Pacific can be explained by the hysteresis of the ITCZ due to the slow ocean circulation adjustment related to cross-equatorial energy exchanges between the Northern and Southern hemispheres⁹.

Although the detailed dynamical process differs between regions, a fundamental mechanism for hysteresis and reversibility can be broadly modelled as an inertia effect. The multi-stability is also a possible mechanism for them^{35–38}, but the inertia effect is a more reasonable hypothesis in this case (Supplementary Discussion 1). The inertia induces a delayed response to CO_2 forcing and can result in hysteresis and irreversible changes. Here we present a simple inertia model for hysteresis and reversibility

$$\frac{dx}{dt} = -\lambda(x - x_{\text{eq}}) \quad (3a)$$

$$x_{\text{eq}} = \alpha F + \beta. \quad (3b)$$

The climate state (x) is restored to equilibrium state (x_{eq}) at the rate of the inertia parameter (λ). The equilibrium state (x_{eq}) depends linearly on the forcing (F) with a sensitivity, α . β is an adjustment parameter for the x_{eq} . λ characterizes the inertia of the system. A small (large) λ induces slow (fast) damping of the x to x_{eq} , resulting in high (low) inertia of the system.

A solution of the simple inertia model is presented in Fig. 5a. The forcing (F) is increased from 367 to 1,468 with 1% per unit model time and decreased back to the initial level with the same rate as a

parallel to the Earth system model experiment (Methods provide details). The parameter is set as $\lambda = 0.02$, $\alpha = 1$ and $\beta = 1$. The solution follows a different trajectory during increasing (orange line in Fig. 5a) and decreasing forcing (blue line in Fig. 5a) and exhibits hysteresis. Also, it does not return to its initial state, showing a difference between final and initial state, Δx . The inertia effect characterized by λ induces such hysteresis and irreversible changes in response to the transient forcing. To examine the effect of λ , the hysteresis area and Δx are calculated with varying λ . As λ increases (or the inertia decreases), both hysteresis area and Δx decreased, converging into zero (black line in Fig. 5b,c). If Δx is sufficiently close to zero ($\Delta x \approx 0$), the response becomes virtually reversible. This theoretical inertia curve provides the baseline to examine the inertia effect on hysteresis area and Δx . A more detailed mathematical discussion is provided in Supplementary Discussion 2.

To examine how well the inertia effect explains the global hysteresis pattern, we compared the Earth system model experiment result with the theoretical inertia curve. For each grid point of the simulated surface temperature and precipitation, the λ is fitted (Supplementary Fig. 6), and normalized hysteresis area and Δx are calculated (Supplementary Figs. 7 and 8). The normalization excludes the effect of α on the hysteresis area and Δx , thus it allows us to directly examine the effect of λ (details can be found in Methods).

The hysteresis area of the surface temperature strongly follows the theoretical inertia curve ($R^2 = 0.84$) (Fig. 5b). The Δx also follows it ($R^2 = 0.65$) with some differences (Fig. 5c). There are two distinct branches on both hysteresis areas and Δx . Most of the globe regions are on the main branch that follows the theoretical inertia curves well. As an exception, the North Atlantic Ocean appears on the secondary branch that does not follow the theoretical inertia curve. In the North Atlantic Ocean, the surface temperature response cannot be explained by the simple inertia model; it gradually warms during the CO_2 ramp up, followed by abrupt cooling and then warming during CO_2 ramp down (Fig. 2c). Physically, the temperature response is associated with the overshooting Atlantic Meridional Overturning Circulation during the CO_2 removal phase^{39,40}.

The hysteresis area of the precipitation weakly follows the theoretical inertia curve ($R^2 = 0.39$) (Fig. 5d), and the Δx does not follow

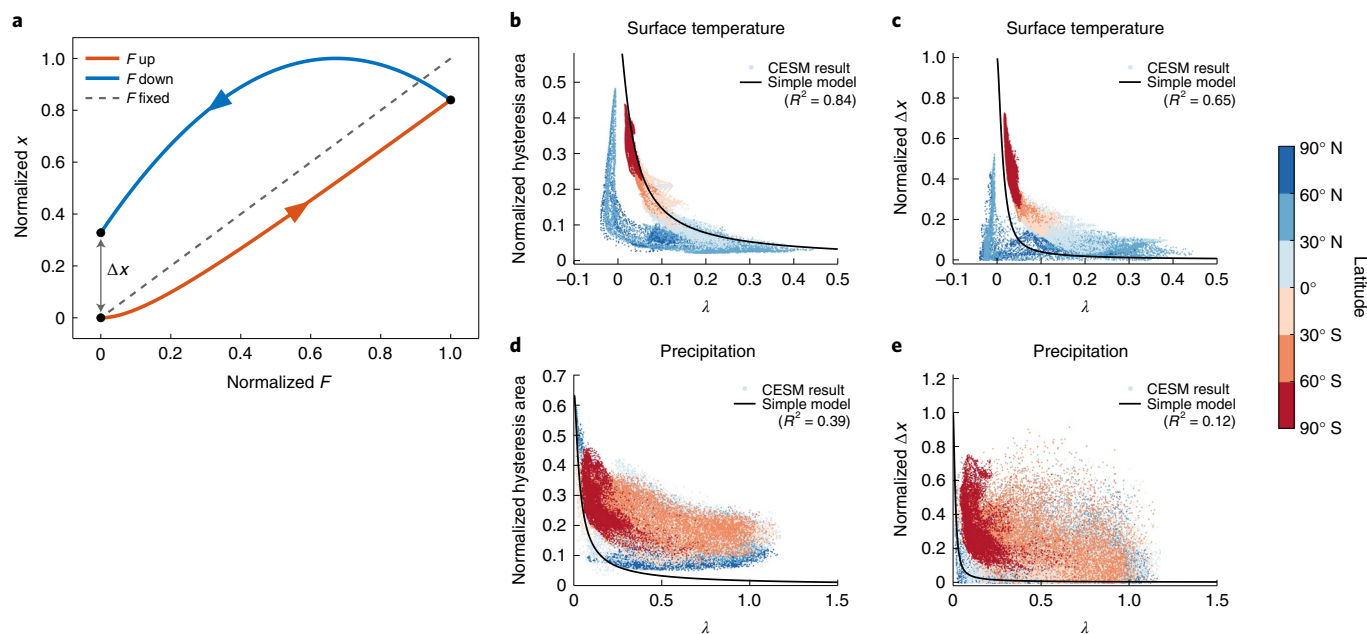


Fig. 5 | The simple inertia model for hysteresis and reversibility. **a**, Solution of the simple inertia model. The x and F correspond to climate state (for example, surface temperature and precipitation) and CO_2 forcing, respectively. They are normalized to have a range of 0 to 1. The trajectory shows the climate trajectory during increasing F (orange line) and decreasing F (blue line). The black dashed line is a static equilibrium solution where F is fixed. **b–e**, Comparison of the theoretical inertia curve with the experiment result. The normalized hysteresis area and Δx are calculated with varying λ using the simple inertia model (thick black line). For each grid point of the experiment output, the λ is fitted and normalized hysteresis area and Δx are calculated (Methods). The dots represent the result for each grid point and the colour shows the latitude of the dot. The results show normalized hysteresis area of surface temperature (**b**) and precipitation (**d**). The result for normalized Δx for surface temperature (**c**) and precipitation (**e**).

the curve as well ($R^2=0.12$) (Fig. 5e). Both exhibit a large scatter around the inertia curve. Previous studies^{12,13} argued that hysteresis of global mean precipitation is attributed to the inertia of the ocean. Outgoing longwave radiation and following the atmosphere's cooling capacity lags in response to greenhouse gas forcing due to a slow ocean heat-uptake process, and it eventually leads to the precipitation hysteresis. Consistent with the previous studies, the simulated trajectory of global mean precipitation coincides with the solution of the simple inertia model (global average panel in Figs. 3c and 5a). However, the inertia effect alone cannot explain the regional pattern of the precipitation hysteresis and reversibility as shown in Figs. 5d and 5e. More complex dynamics need to be introduced to explain the diverse response patterns over regions. In particular, non-local processes should be accounted for, such as deep convection over high sea surface temperature (SST) in tropics⁴¹ and storm tracks sensitive to horizontal SST gradients.

Discussion

The widespread hysteresis over the globe may induce hysteresis in diverse parts of the climate system. For example, the climate hysteresis in the Himalayas and Arctic can affect mountain glaciers⁴² and summer sea ice^{43–45}, respectively, and the hysteresis in the Amazon can influence the rainforest⁴⁶.

The results presented in this paper are based on a forcing scenario that varies CO_2 concentration levels at a rate of 1% per year following the standard protocol of the Carbon Dioxide Removal Model Intercomparison Project² (Supplementary Fig. 9). The regional patterns of hysteresis and reversibility would depend on the rate of forcing (Supplementary Figs. 10 and 11). So far, the additional rate-sensitivity experiment showed that the surface temperature hysteresis responses over the Southern Ocean, North Atlantic and Arctic vary with the forcing rate (Supplementary Fig. 10), while the precipitation hysteresis is less sensitive to the rate of forcing

(Supplementary Fig. 11). The dependency of regional climate hysteresis on the forcing rate needs to be further explored in the future.

Our quantification method can be universally applicable for any type of climate variable and forcing scenario, facilitating an understanding of regional patterns of hysteresis and reversibility. Further, the original definitions presented in this paper can be extended or modified; for example, the reversibility can be measured as Δx instead of openness of the loop to quantify the reversibility with more detail.

Our results show that the influence of greenhouse gas is not confined to the current warming period, and it extends beyond the human-perceptible timescale. Even after it is completely restored to the pre-industrial level, the climate may not be reversible in most regions, especially over many developing countries.

Online content

Any methods, additional references, Nature Research reporting summaries, source data, extended data, supplementary information, acknowledgements, peer review information; details of author contributions and competing interests; and statements of data and code availability are available at <https://doi.org/10.1038/s41558-022-01452-z>.

Received: 21 January 2022; Accepted: 18 July 2022;
Published online: 1 September 2022

References

- Osman, M. B. et al. Globally resolved surface temperatures since the Last Glacial Maximum. *Nature* **599**, 239–244 (2021).
- Keller, D. P. et al. The Carbon Dioxide Removal Model Intercomparison Project (CDRMIP): rationale and experimental protocol for CMIP6. *Geosci. Model Dev.* **11**, 1133–1160 (2018).
- Rahmstorf, S. et al. Thermohaline circulation hysteresis: a model intercomparison. *Geophys. Res. Lett.* **32**, 1–5 (2005).

4. Hawkins, E. et al. Bistability of the Atlantic overturning circulation in a global climate model and links to ocean freshwater transport. *Geophys. Res. Lett.* **38**, L10605 (2011).
5. An, S.-I., Kim, H.-J. & Kim, S.-K. Rate-dependent hysteresis of the Atlantic Meridional Overturning Circulation system and its asymmetric loop. *Geophys. Res. Lett.* **48**, e2020GL090132 (2021).
6. Pollard, D. & DeConto, R. M. Hysteresis in Cenozoic Antarctic ice-sheet variations. *Glob. Planet. Change* **45**, 9–21 (2005).
7. Garbe, J., Albrecht, T., Levermann, A., Donges, J. F. & Winkelmann, R. The hysteresis of the Antarctic ice sheet. *Nature* **585**, 538–544 (2020).
8. Ohba, M., Tsutsui, J. & Nohara, D. Statistical parameterization expressing ENSO variability and reversibility in response to CO₂ concentration changes. *J. Clim.* **27**, 398–410 (2014).
9. Kug, J.-S. et al. Hysteresis of the intertropical convergence zone to CO₂ forcing. *Nat. Clim. Change* **12**, 47–53 (2022).
10. Song, S. Y. et al. Asymmetrical response of summer rainfall in East Asia to CO₂ forcing. *Sci. Bull.* **67**, 213–222 (2022).
11. Boucher, O. et al. Reversibility in an Earth system model in response to CO₂ concentration changes. *Environ. Res. Lett.* **7**, 024013 (2012).
12. Wu, P., Wood, R., Ridley, J. & Lowe, J. Temporary acceleration of the hydrological cycle in response to a CO₂ rampdown. *Geophys. Res. Lett.* **37**, L12705 (2010).
13. Cao, L., Bala, G. & Caldeira, K. Why is there a short-term increase in global precipitation in response to diminished CO₂ forcing? *Geophys. Res. Lett.* **38**, L06703 (2011).
14. MacDougall, A. H. Reversing climate warming by artificial atmospheric carbon-dioxide removal: can a Holocene-like climate be restored? *Geophys. Res. Lett.* **40**, 5480–5485 (2013).
15. Wu, P., Ridley, J., Pardaens, A., Levine, R. & Lowe, J. The reversibility of CO₂ induced climate change. *Clim. Dyn.* **45**, 745–754 (2015).
16. Tokarska, K. B. & Zickfeld, K. The effectiveness of net negative carbon dioxide emissions in reversing anthropogenic climate change. *Environ. Res. Lett.* **10**, 094013 (2015).
17. Zickfeld, K., MacDougall, A. H. & Damon Matthews, H. On the proportionality between global temperature change and cumulative CO₂ emissions during periods of net negative CO₂ emissions. *Environ. Res. Lett.* **11**, 055006 (2016).
18. Chadwick, R., Wu, P., Good, P. & Andrews, T. Asymmetries in tropical rainfall and circulation patterns in idealised CO₂ removal experiments. *Clim. Dyn.* **40**, 295–316 (2013).
19. Lehner, F. & Stocker, T. F. From local perception to global perspective. *Nat. Clim. Change* **5**, 731–734 (2015).
20. Seneviratne, S. I., Donat, M. G., Pitman, A. J., Knutti, R. & Wilby, R. L. Allowable CO₂ emissions based on regional and impact-related climate targets. *Nature* **529**, 477–483 (2016).
21. Jeltsch-Thömmes, A., Stocker, T. F. & Joos, F. Hysteresis of the Earth system under positive and negative CO₂ emissions. *Environ. Res. Lett.* **15**, 124026 (2020).
22. Scheffer, M. et al. Early-warning signals for critical transitions. *Nature* **461**, 53–59 (2009).
23. Schneider, T., Bischoff, T. & Haug, G. H. Migrations and dynamics of the intertropical convergence zone. *Nature* **513**, 45–53 (2014).
24. Alfonso, H. et al. *World Economic Situation and Prospects: Report 2021* (Department of Economic and Social Affairs, United Nations, 2021).
25. Mertz, O., Halsnæs, K., Olesen, J. E. & Rasmussen, K. Adaptation to climate change in developing countries. *Environ. Manage.* **43**, 743–752 (2009).
26. Cai, Y., Judd, K. L. & Lontzek, T. S. *The Social Cost of Stochastic and Irreversible Climate Change* NBER Working Paper (National Bureau of Economic Research, 2013); <https://econpapers.repec.org/RePEc:nbr:nberwo:18704>
27. Cai, Y. & Lontzek, T. S. The social cost of carbon with economic and climate risks. *J. Polit. Econ.* **127**, 2684–2734 (2019).
28. Robinson, A., Calov, R. & Ganopolski, A. Multistability and critical thresholds of the Greenland ice sheet. *Nat. Clim. Change* **2**, 429–432 (2012).
29. Hall, A. The role of surface albedo feedback in climate. *J. Clim.* **17**, 1550–1568 (2004).
30. Smetacek, V. & Nicol, S. Polar ocean ecosystems in a changing world. *Nature* **437**, 362–368 (2005).
31. Schofield, O. et al. How do polar marine ecosystems respond to rapid climate change? *Science* **328**, 1520–1523 (2010).
32. Li, C., von Storch, J. S. & Marotzke, J. Deep-ocean heat uptake and equilibrium climate response. *Clim. Dyn.* **40**, 1071–1086 (2013).
33. Long, S.-M., Xie, S.-P., Zheng, X.-T. & Liu, Q. Fast and slow responses to global warming: sea surface temperature and precipitation patterns. *J. Clim.* **27**, 285–299 (2014).
34. Armour, K. C., Marshall, J., Scott, J. R., Donohoe, A. & Newsom, E. R. Southern Ocean warming delayed by circumpolar upwelling and equatorward transport. *Nat. Geosci.* **9**, 549–554 (2016).
35. Stommel, H. Thermohaline convection with two stable regimes of flow. *Tellus* **13**, 224–230 (1961).
36. Budyko, M. I. The effect of solar radiation variations on the climate of the Earth. *Tellus* **21**, 611–619 (1969).
37. Held, I. M. & Suarez, M. J. Simple albedo feedback models of the icecaps. *Tellus* **26**, 613–629 (1974).
38. Watson, A. J. & Lovelock, J. E. Biological homeostasis of the global environment: the parable of Daisyworld. *Tellus B* **35**, 284–289 (1983).
39. Wu, P., Jackson, L., Pardaens, A. & Schaller, N. Extended warming of the northern high latitudes due to an overshoot of the Atlantic meridional overturning circulation. *Geophys. Res. Lett.* **38**, L24704 (2011).
40. An, S.-I. et al. Global cooling hiatus driven by an AMOC overshoot in a carbon dioxide removal scenario. *Earths Future* **9**, e2021EF002165 (2021).
41. Xie, S.-P. et al. Global warming pattern formation: sea surface temperature and rainfall. *J. Clim.* **23**, 966–986 (2010).
42. Shrestha, A. B. & Aryal, R. Climate change in Nepal and its impact on Himalayan glaciers. *Reg. Environ. Change* **11**, 65–77 (2011).
43. Merryfield, W. J., Holland, M. M. & Monahan, A. H. in *Arctic Sea Ice Decline: Observations, Projections, Mechanisms, and Implications* (eds DeWeaver, E. T. et al.) 151–174 (American Geophysical Union, 2008).
44. Luo, B., Luo, D., Wu, L., Zhong, L. & Simmonds, I. Atmospheric circulation patterns which promote winter Arctic sea ice decline. *Environ. Res. Lett.* **12**, 054017 (2017).
45. Olonscheck, D., Mauritsen, T. & Notz, D. Arctic sea-ice variability is primarily driven by atmospheric temperature fluctuations. *Nat. Geosci.* **12**, 430–434 (2019).
46. Staal, A. et al. Hysteresis of tropical forests in the 21st century. *Nat. Commun.* **11**, 4978 (2020).

Publisher's note Springer Nature remains neutral with regard to jurisdictional claims in published maps and institutional affiliations.



Open Access This article is licensed under a Creative Commons Attribution 4.0 International License, which permits use, sharing, adaptation, distribution and reproduction in any medium or format, as long as you give appropriate credit to the original author(s) and the source, provide a link to the Creative Commons license, and indicate if changes were made. The images or other third party material in this article are included in the article's Creative Commons license, unless indicated otherwise in a credit line to the material. If material is not included in the article's Creative Commons license and your intended use is not permitted by statutory regulation or exceeds the permitted use, you will need to obtain permission directly from the copyright holder. To view a copy of this license, visit <http://creativecommons.org/licenses/by/4.0/>.

© The Author(s) 2022

Methods

Experiment configuration and design. We conducted the CO₂ ramp-up and ramp-down experiment using the Community Earth System Model version 1.2 (ref. ⁴⁷) (CESM1.2). The model is composed of the atmosphere (Community Atmospheric Model version 5), ocean (Parallel Ocean Program version 2), sea ice (Community Ice Code version 4) and land models (Community Land Model version 4). The atmospheric model has a horizontal resolution of approximately 1° and 30 vertical levels⁴⁸. The ocean model has 60 vertical levels, with a longitudinal resolution of 1° and a gradually changing latitudinal resolution of 1/3° near the equator to 1/2° near the poles⁴⁹. The land model includes the carbon–nitrogen cycle⁵⁰.

The experiment was performed with idealized CO₂ scenarios composed of two different phases (Supplementary Fig. 9). In the first phase, the atmospheric CO₂ concentration level is fixed at 367 ppm as a present-day level, and the experiment is run for 900 years with a single ensemble (PD period). Before the PD period, the model is spun up for 800 years. In the second phase, the CO₂ concentration level increased from 367 ppm to 1,478 ppm at a rate of 1% per year for 140 years (ramp-up period), then decreased back to 367 ppm at the same rate for 140 years (ramp-down period). Followed by the ramp-down period, the CO₂ level is fixed at 367 ppm for 220 years (restoring period). The second phase experiment is run with 28 ensemble members with different initial conditions, which are extracted from the PD period. The initial conditions are set to have different phases of the multi-decadal climate oscillations such as the Atlantic Multidecadal Oscillation and Pacific Decadal Oscillation.

Calculation of the hysteresis area and openness. We calculated the hysteresis area and openness of the loop for each grid point of surface temperature and precipitation. We used ensemble mean surface temperature and precipitation. The ensemble mean can filter out the internal variability and show forced response to CO₂ forcing. The calculation covers CO₂ ramp-up and ramp-down periods. To remove high-frequency fluctuation, we applied a moving mean filter of 21 years.

The hysteresis area was calculated by equation (1) using the trapezoidal numerical integration method. The openness of the loop was calculated by a different but stricter definition than the one introduced in the main text (equation (2)). In the main text, for simplicity, we implicitly assumed that the trajectories during CO₂ ramp up (x_{up}) and ramp down (x_{down}) do not intersect each other, and they can only meet at the lowest level of CO₂ ($F_{present}$) only if the loop is closed (Fig. 1). However, in the several grid points of experimental output, the trajectories intersect at the intermediate level of CO₂ and exhibit a twisted curve shape. Such a type of loop is reasonable to be read as a closed-loop (reversible response) although it is characterized as open-loop by the definition in the main text (equation (2)). To account for these cases, we calculated the openness of the loop using a refined definition as follows:

$$\text{Loop} = \begin{cases} \text{Open for } \min(x_{up}^* - x_{down}^*) \times \max(x_{up}^* - x_{down}^*) > 0 \\ \text{Closed for } \min(x_{up}^* - x_{down}^*) \times \max(x_{up}^* - x_{down}^*) \leq 0 \end{cases} \quad (4)$$

where x_{up}^* and x_{down}^* are ramp-up and ramp-down trajectories during a range of CO₂ levels from $F_{present}$ to F_{mid} , respectively. This definition classifies a trajectory as closed-loop (open-loop) if x_{up}^* and x_{down}^* (do not) intersect during specific range of CO₂ levels from $F_{present}$ to F_{mid} . The $F_{present}$ is 367 ppm by the CO₂ scenarios in our experiment, and we selected F_{mid} as 1,300 ppm. We directly applied the refined definition (equation (4)) to the processed experiment output.

Detecting hotspots of irreversible changes. The hotspot of irreversible changes is detected based on the annual mean land surface temperature and precipitation. The hotspot is defined as the land area where both surface temperature and precipitation show open-loop response and hysteresis area larger than its 50th percentile.

Solving the simple inertia model. The simple inertia model (equations (3a) and (3b)) was solved using the Euler time integration method with a time interval, $dt=0.01$. The forcing, $F(t)$ was imposed as:

$$F(t) = \begin{cases} F_0 r^t & \text{for } 0 \leq t < T/2 \\ F_0 r^{(T-t)} & \text{for } T/2 \leq t < T \end{cases} \quad (5)$$

where $F_0=367$, $r=1.01$, $T=280$ as a parallel to the Earth system model experiment. The model parameters are set as $\lambda=0.02$, $\alpha=1$ and $\beta=0$. The initial condition of x was set to F_0 . All quantities are dimensionless. To obtain the theoretical baseline of the inertia effect (black lines in Fig. 5b–e), we calculated the normalized hysteresis area and Δx with varying λ . The normalized hysteresis area and Δx were calculated using the normalized x and F that have a range of 0 to 1.

Linking the simple inertia model to the experiment result. The hysteresis area and Δx of the surface temperature and precipitation were compared with the theoretical baseline obtained from the simple inertia model (black lines in Fig. 5b–e). The λ was fitted for each grid point of the surface temperature and precipitation (Supplementary Fig. 6). We used normalized surface temperature, precipitation and CO₂ concentration levels that have a range of 0 to 1. Substitute equation (3b) to equation (3a) and discretize $\frac{dx}{dt}$ term with forward Euler scheme:

$$\frac{x_{i+1} - x_i}{\Delta t} = -\lambda x_i + \lambda \alpha F_i + \lambda \beta \quad (6)$$

where $\Delta t=1$ year and subscript i indicates i th time-step point ($i=1, 2, \dots, 279$). We performed linear regression for equation (6) and estimated λ .

The normalized hysteresis area and Δx were calculated using the normalized x and F (Supplementary Figs. 7 and 8). The normalization can exclude the effect of α on hysteresis area and Δx ; thus, it allows us to directly compare the Earth system model experiment result with the theoretical inertia baseline.

Specifically, α linearly scales the hysteresis area and Δx . If α increases k times, both hysteresis area and Δx increase k times as well. β does not affect the hysteresis area and Δx at all; thus, we don't have to consider it (Supplementary Discussion 2). Thus, the effect of α on hysteresis area and Δx should be excluded to solely examine the effect of λ . To eliminate its effect, for each grid point, we performed the normalization that linearly transforms x and F to have a range of 0 to 1. It is essentially equivalent to setting $\alpha=1$ for all grid points; thus, the normalization excludes the effect of α on the hysteresis area and Δx .

Data availability

The data used in this paper are available from <https://doi.org/10.6084/m9.figshare.20289123.v2>⁵¹.

Code availability

The code for the simple inertia model simulation is available from <https://doi.org/10.6084/m9.figshare.20290017.v4>⁵².

References

- Hurrell, J. W. et al. The community earth system model: a framework for collaborative research. *Bull. Am. Meteorol. Soc.* **94**, 1339–1360 (2013).
- Neale, R. B. et al. *Description of the NCAR Community Atmosphere Model (CAM 5.0)* NCAR Technical Note NCAR/TN-486+STR (National Center of Atmospheric Research, 2012).
- Smith, R. et al. *The Parallel Ocean Program (POP) Reference Manual Ocean Component of the Community Climate System Model (CCSM) and Community Earth System Model (CESM)* Rep. LAUR-01853 (UCAR, 2010)
- Lawrence, D. M. et al. Parameterization improvements and functional and structural advances in version 4 of the Community Land Model. *J. Adv. Model. Earth Syst.* **3**, M03001 (2011).
- Kim, S.-K. et al. Data for “Widespread irreversible changes in surface temperature and precipitation in response to CO₂ forcing”. *figshare* <https://doi.org/10.6084/m9.figshare.20289123.v2> (2022).
- Kim, S.-K. et al. Code for “Widespread irreversible changes in surface temperature and precipitation in response to CO₂ forcing”. *figshare* <https://doi.org/10.6084/m9.figshare.20290017.v4> (2022).

Acknowledgements

We are grateful to D. Kim for stimulating the discussion of the research. This work was supported by the National Research Foundation of Korea (NRF) grant funded by the Korea government (MSIT) (NRF-2018R1A5A1024958) and Yonsei Signature Research Cluster Program of 2021 (2021-22-0003). The CESM simulation was carried out on the supercomputer supported by the National Center for Meteorological Supercomputer of Korea Meteorological Administration (KMA), the National Supercomputing Center with supercomputing resources, associated technical support (KSC-2019-CHA-0005) and the Korea Research Environment Open NETwork (KREONET).

Author contributions

S.-K.K. conceived the idea of the research and drafted the article. S.-K.K. developed the conceptual framework for hysteresis and reversibility inspired by group discussion with J.S., H.-J.K., and N.I. J.S. conducted the Earth system model experiment. S.-K.K. and J.S. performed the post-data processing of the experiment output. S.-K.K. established the simple inertia model and performed the analysis on it. J.S. assisted the analysis. S.-K.K. prepared the figures by discussing with J.S. and S.-I.A. N.I. assisted in the illustration for Fig. 1. J.S. assisted in figure configuration for Fig. 2 and Fig. 3. S.-I.A. oversaw the project. All the authors discussed the results and wrote the article.

Competing interests

The authors declare no competing interests.

Additional information

Supplementary information The online version contains supplementary material available at <https://doi.org/10.1038/s41558-022-01452-z>.

Correspondence and requests for materials should be addressed to Soon-Il An.

Peer review information *Nature Climate Change* thanks Kirsten Zickfeld and the other, anonymous, reviewer(s) for their contribution to the peer review of this work.

Reprints and permissions information is available at www.nature.com/reprints.